

# Empirical model of SSUSI-derived auroral ionization rates

Stefan Bender<sup>1,2,3</sup>, Patrick J. Espy<sup>2,3</sup>, Larry J. Paxton<sup>4</sup>

<sup>1</sup>Instituto de Astrofísica de Andalucía (CSIC), Granada, Spain

<sup>2</sup>Department of Physics, Norwegian University of Science and Technology, Trondheim, Norway

<sup>3</sup>Birkeland Centre for Space Science, Bergen, Norway

<sup>4</sup>Applied Physics Laboratory, Johns Hopkins University, Laurel, Maryland, USA

## Key Points:

- We present an empirical model for auroral ionization rates between 90 and 150 km derived from SSUSI FUV observations.
- The model is based on linear regression with respect to the geomagnetic Kp, PC, and Ap indices, and the solar F10.7 radio flux.
- We find that Kp captures the largest fraction of the ionization rate variability.

arXiv:2312.11130v2 [physics.ao-ph] 2 Dec 2024

---

Corresponding author: Stefan Bender, [sbender@iaa.es](mailto:sbender@iaa.es)

## Abstract

We present an empirical model for auroral (90–150 km) electron–ion pair production rates, ionization rates for short, derived from SSUSI (Special Sensor Ultraviolet Spectrographic Imager) electron energy and flux data. Using the Fang et al. (2010) parametrization for mono-energetic electrons, and the NRLMSISE-00 neutral atmosphere model (Picone et al., 2002), the calculated ionization rate profiles are binned in 2-h magnetic local time (MLT) and  $3.6^\circ$  geomagnetic latitude to yield time series of ionization rates at 5-km altitude steps. We fit each of these time series to the geomagnetic indices Kp, PC, and Ap, the 81-day averaged solar  $F_{10.7}$  radio flux index, and a constant term. The resulting empirical model can easily be incorporated into coupled chemistry–climate models to include particle precipitation effects.

## Plain Language Summary

Aurorae or polar lights are produced at around 100 km at high latitudes by electrons and protons from space that enter the upper atmosphere, approximately around  $65^\circ$  North and South. Besides creating beautiful auroral displays, these particles also change the atmospheric composition by ionizing the air and thus initiating chemical reactions. Chemistry–climate models have recently started implementing these changes in their simulations. However, so far these simulations do not match observations. One possible reason is that the input for the models is based on satellite observations of particles far above 100 km, without knowing exactly how many of them enter the atmosphere. Here we present a way to use space observations of the aurora to calculate the number of particles actually entering the atmosphere. We use these aurora observations to construct a mathematical formula to calculate how much of the atmosphere is ionized by the electrons and protons. Our formula is based on indices of geomagnetic activity, and it can be used in more complicated chemistry–climate models to better incorporate these effects in their simulations.

## 1 Introduction

Particle precipitation and the associated processes initiated in the middle and upper atmosphere have been recognized as one component of natural climate variability and are included in the most recent climate prediction simulations initiated by the Intergovernmental Panel on Climate Change (IPCC) (Matthes et al., 2017). So far, most of the model inputs are based on in-situ particle observations at satellite orbital altitudes ( $\approx 800$  km) (e.g. Wissing & Kallenrode, 2009; van de Kamp et al., 2016; Smith-Johnsen et al., 2018), or on trace-gas observations (Randall et al., 2009; Funke et al., 2017). In addition, most recent studies focus on the influence of “medium-energy” electrons (MEE) (30–1000 keV) (Smith-Johnsen et al., 2018; Tyssøy et al., 2021; Sinnhuber et al., 2021) that have their largest impact in the mesosphere ( $\lesssim 90$  km). But all three of these studies have *also* found a considerable discrepancy between observations and models regarding the nitric oxide (NO) content in the *lower thermosphere* (100–120 km). In the latest studies by Tyssøy et al. (2021) and Sinnhuber et al. (2021), this part of the atmosphere is modelled using total energy flux and an auroral-oval parametrization based on Kp, or using ionization rates provided by the Atmosphere Ionization Module Osnabrück (AIMOS; Wissing and Kallenrode (2009)), which is derived from aforementioned in-situ particle observations. However, inferring the flux precipitating into the atmosphere from the in-situ particle measurements has its own difficulties and uncertainties, for example determining the loss cone (Tyssøy et al., 2016).

In addition to the direct ionization and chemical impact of MEE on the mesosphere, the descent of NOx from the lower thermosphere to the stratosphere has been observed (Randall et al., 2009; Funke et al., 2005, 2014). This transport happens regularly during the final warming and the breakup of the polar vortex in late winter and spring, and during

Sudden Stratospheric Warmings with Elevated-Stratopause events (Pérot et al., 2014; Pérot & Orsolini, 2021). This indirect source of NO<sub>x</sub> in the middle atmosphere has its origin in the auroral production of NO in the lower thermosphere. So far this auroral NO source is mostly described by simple parametrizations in whole-atmosphere chemistry-climate models (Sinnhuber et al., 2021), with the exception of AIMOS which is derived from POES particle flux measurements (Wissing & Kallenrode, 2009). Although the model comparison study by Sinnhuber et al. (2021) found good agreement of auroral NO with data *on average*, the amounts differ by an order of magnitude between the individual models. Our model adds another approach to modelling this auroral NO source in global climate models, derived from direct auroral UV emission observations.

The Special Sensor Ultraviolet Spectrographic Imagers (SSUSI) are UV imagers (115–180 nm) on board the Defense Meteorological Satellite Program (DMSP) Block-5D3 satellites F17 and F18 (Paxton et al., 1992, 2017, 2018). These instruments picture approximately 3000 km wide swaths of both auroral zones with a pixel resolution of 10×10 km at the nadir point. By observing the atmospheric emissions directly, this avoids the problem of having to model the input into the atmosphere as is the case with the aforementioned in-situ particle measurements.

From these data we derived ionization rate profiles (Bender et al., 2021), and here we develop an empirical regression model of these rates binned in magnetic local time (MLT) and geomagnetic latitude. The model uses 4 geomagnetic and solar activity indicators: the geomagnetic Kp and Ap indices, the auroral Polar Cap (PC) index, and the 81-day centred moving average of the solar 10.7-cm radio flux. Our model complements the existing ionization rate models for higher-energetic electrons such as ApEEP (van de Kamp et al., 2016, 2018); it is also based on geomagnetic indices and ready to use in chemistry-climate models that include the upper atmosphere. The intended main purpose of our model is to drive the auroral ionization input in the lower thermosphere in whole-atmosphere chemistry-climate models. Furthermore, the presented model provides the uncertainties in the proxy coefficients which can be used to estimate the uncertainty in the modelled ionization rates. Those can be further used to carry out statistical ensemble runs of chemistry-climate models, randomly driven by the ionization rates within their uncertainties.

The paper is organized as follows: the data and processing steps are described in Sect. 2, the model setup is laid out in Sect. 3, and the results are presented in Sect. 4.

## 2 Data

We use the electron energy and energy flux data from the Special Sensor Ultraviolet Spectrographic Imager (SSUSI) instruments on board the Defense Meteorological Satellite Program (DMSP) Block-5D3 satellites F17 and F18 (Paxton et al., 1992, 2017, 2018). These satellites orbit at 850 km altitude in polar, sun-synchronous orbits, the equator crossing times of their ascending nodes are 17:34 LT (F17) and 20:00 LT (F18). The orbital period is of the order of 100 min, resulting in about 15 orbits per day. These instruments provide about 3000 km-wide spectrographic images of the auroral zones with a 10 km×10 km pixel size at the nadir point. For bandwidth reasons, they downlink 5 UV channels including two colours for the LBH (Lyman–Birge–Hopfield) band emissions of N<sub>2</sub>. From these two LBH colours the electron energies and energy fluxes are derived based on Strickland et al. (1983), and an extensive discussion can be found in Knight et al. (2018). The electron energy and flux data we use here are provided within the Auroral-EDR (Environmental Data Record) data set at [https://ssusi.jhuapl.edu/data\\_products](https://ssusi.jhuapl.edu/data_products) (SSUSI, 2020).

For each pixel we calculate the ionization rate (IR) profile as described in (Bender et al., 2021) for altitudes 90–150 km. Briefly, we use the parametrization by (Fang et al., 2010) for mono-energetic electrons and integrate over a Maxwellian spectrum for mag-

netic local times (MLT)  $\leq 12:00$  and over a Gaussian spectrum for  $\text{MLT} > 12:00$  as determined by our comparison study (Bender et al., 2021). We use NRLMSISE-00 (Picone et al., 2002) for the background neutral atmosphere, calculated at each pixel location. By converting the ionization rates to electron densities, these data have previously been validated against EISCAT ground-based measurements (Bender et al., 2021).

### 3 Model description

We bin the ionization rate profiles from the SSUSI data in 2-h magnetic local time (MLT) bins from 00:00–02:00 MLT to 22:00–00:00(+1 d) MLT and in  $3.6^\circ$  geomagnetic latitude bins from  $52.2^\circ$  ( $50.4\text{--}54.0^\circ$ ) to  $88.2^\circ$  ( $86.4\text{--}90.0^\circ$ ) in both hemispheres. In each bin the ionization rate profiles are calculated using the parametrization by Fang et al. (2010) on a 5-km altitude grid from 90 to 150 km, evaluated directly for the given altitude  $z$ . The spectra are used according to the validation study by Bender et al. (2021). We chose to average the profiles instead of the energy and fluxes because converting them to ionization rates is highly non-linear in electron energy (Fang et al., 2010). This approach has the advantage that mixed spectra are better represented in the final ionization input which are hard to capture with average parameters. For example the case of a mixture of two Maxwellian-type spectra as presented in Fang et al. (2010, Fig. 4); the average has no analytical representation and even using a different kind of spectra is unable to reproduce the mixed spectrum fully. As a result, the alternative approaches fail to reproduce the “double-peak” structure of the ionization rate profile, which can be retained to some extent by using the average profile instead of the average parameters.

In each bin the vertical profiles are averaged per orbit, yielding a time series of ionization rates  $q$  with a standard deviation for every 5-km altitude step. To reduce the low bias introduced by orbits with very few non-zero ionization rate data points in the respective grid cell, we omit the data from those orbits where the average  $q$  is smaller than 0.001 times the median of the time series. We use these time series in each bin to fit a multi-linear regression model to  $\log(q)$ <sup>1</sup> as follows:

$$\log(q) = a \cdot \text{Kp} + b \cdot \text{PC} + c \cdot \text{Ap} + d \cdot \log(\overline{\text{F}_{10.7}}) + \text{const.} + \varepsilon. \quad (1)$$

In Eq. (1), Kp and Ap are the 3-h geomagnetic indices (e.g. Manda & Korte, 2011), PC is the 1-h polar cap index (Troshichev et al., 1979, 1988),  $\overline{\text{F}_{10.7}}$  is the 81-day moving average of the solar 10.7 cm radio flux, centred on the day to be fitted. This list of proxies has been empirically determined by iterating the available options and where feasible their natural logarithm, adding one by one and keeping those with the best fit in terms of maximum likelihood. The iteration was stopped when further improvement in terms of the “Bayesian Information Criterion” (see, e.g. Wit et al., 2012) did not justify adding another regressor to the list. That is, the proxies in Eq. (1) are ordered by (empirical) relevance. All the indices are taken from the OMNI space weather index database (King & Papitashvili, 2005) and hourly-sampled values are used (Papitashvili & King, 2020). We use Bayesian linear regression with conjugate priors to fit the model coefficients. We use a wide normal distribution around zero ( $\sigma = 10$ ) as the prior distribution for the coefficients, and a wide inverse Gamma distribution ( $\alpha = 1, \beta = 1$ ) as the prior distribution for the variance.

Note that because of the F17 and F18 orbits, not all latitude/MLT bins are sampled equally. Therefore, in bins with low number of points, that is with less than 240 data points, we use bilinear interpolation in MLT and geomagnetic latitude to calculate the coefficient.

---

<sup>1</sup> Unless stated otherwise,  $\log()$  denotes the natural logarithm as the inverse of the exponential  $\exp()$  which is defined by the solution of  $\frac{d}{dx} \exp(x) = \exp(x)$  with  $\exp(0) = 1$ .

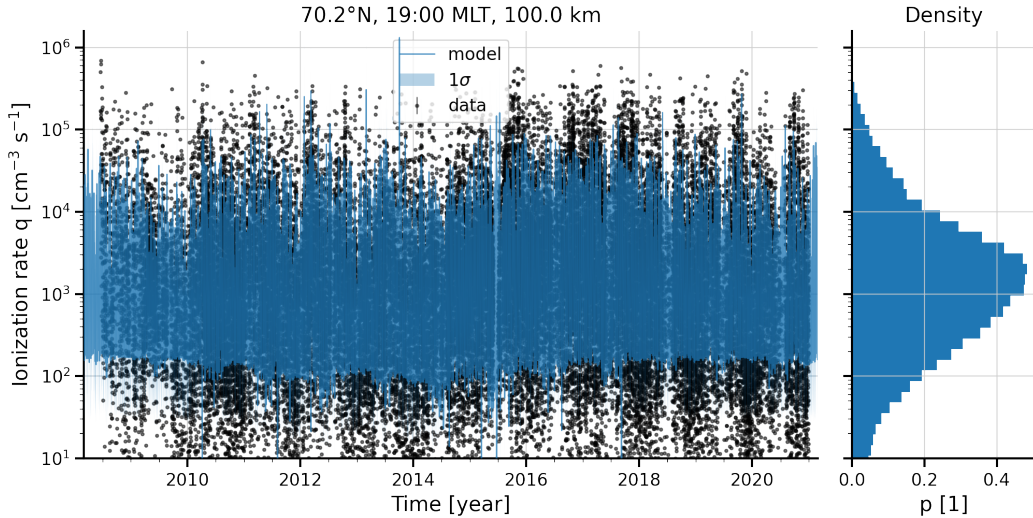


**Figure 1.** Data and model fit for example bin: 19:00 MLT, 70.2°N geomagnetic latitude, 100 km altitude. The histogram shows the distribution of the data.

## 4 Results

### 4.1 Time series fit

We demonstrate the fit quality on an example time series of the model bin centred at 19:00 MLT (18:00–20:00 MLT), 70.2°N geomagnetic latitude (68.4–72.0°N), and at 100 km altitude. This constitutes an example where we have almost 60000 data points available, and it served as a testbed for determining the proxies used as regressors in the model. Note that because of the large range of ionization rates from  $< 1$  to  $10^6 \text{ cm}^{-3} \text{ s}^{-1}$ , the better choice for fitting is  $\log(q)$ .

The data in that bin, together with the model fit, are shown in Fig. 1. The residuals and the  $1\sigma$  prediction uncertainty are shown in Fig. 2. The overall average ionization rate is around  $10^3 \text{ cm}^{-3} \text{ s}^{-1}$ . The fit line indicates a slight variation following approximately an 11-year solar cycle. On top of that, annual and semi-annual variations are visible in the data. Although we do not explicitly include (semi)annual harmonics in the model, they seem to be captured by the combination of the proxies used. Both histograms in Figs. 1 and 2, showing  $\log(q)$  and the residuals, show smooth, almost symmetric distributions. Thus, the assumption of normal-distributed errors for multi-linear regression is satisfied.

### 4.2 Coefficient distributions in the Northern Hemisphere

The fit coefficients in the Northern Hemisphere for 100 km altitude are shown in Fig. 3. The coefficients for Kp and PC show similar patterns, both have their largest effect in a wide band around auroral geomagnetic latitudes, between about 55° and 75° with a maximum around 65°. This similarity suggests that PC accounts for shorter variations (1-h) on top of the 3-h variations captured by Kp, and essentially both describe the same processes. We also observe that the Ap coefficients exhibit a similar pattern, albeit with a negative sign compared to Kp and PC. This may be a sign that the quasi-logarithmic scale of Kp introduces larger changes that are compensated by the linear scale of Ap. The circular patterns in Kp and Ap closer to the pole for MLT 06:00–18:00 are most likely related to cusp precipitation (Newell et al., 2005, 2009). Over almost the entire polar cap, the F10.7 coefficients are distributed opposite to the constant offset co-

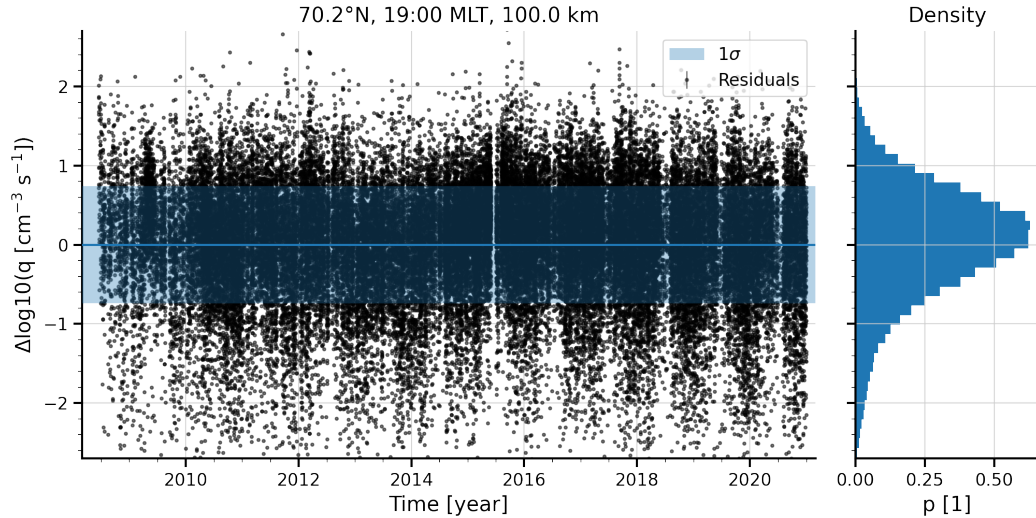


**Figure 2.** Residuals for example bin: 19:00 MLT, 70.2°N geomagnetic latitude, 100 km altitude. The histogram shows the distribution of the residuals.

efficients. This indicates that the influence of the solar cycle is marginal, but it reduced the fitting metric just enough to warrant its inclusion.

### 4.3 Coefficient distributions in the Southern Hemisphere

The fit coefficients in the Southern Hemisphere for 100 km altitude are shown in Fig. 4. The coefficients in the Southern Hemisphere exhibit essentially the same patterns as in the Northern Hemisphere. The coefficients of the geomagnetic indices are of the same magnitude as in the Northern Hemisphere, with slight differences in the MLT/latitude distributions. For PC the extent of positive coefficients is larger in latitude than in the Northern Hemisphere. These small differences could be a sign that the precipitation is not fully symmetric in geomagnetic latitude between North and South, and may also be the result of the geomagnetic indices being almost exclusively derived from observations in the Northern Hemisphere.

### 4.4 Profile comparison to data and AISstorm

The overall performance of the model is difficult to assess based on individual profiles because of its average nature. As shown for example in Fig. 2, the residual variation is still large and for single days, the modelled ionization rates can differ considerably from the data. In Fig. 6, we compare the modelled ionization rate profiles to the original data during the event in April 2010 investigated in previous studies (Tyssøy et al., 2021; Sinnhuber et al., 2021). For this comparison we picked a single geomagnetic latitude/MLT bin, corresponding to 70.2°S and 19:00 MLT. During these three days, the average geomagnetic indices were  $\overline{K_p}$ : 2.6, 4.8, 4.8,  $\overline{PC}$ : 1.8, 3.9, 4.4,  $\overline{A_p}$ : 12.9, 54.6, 43.5, and an approximately constant  $\overline{F_{10.7}}$  of 79 ( $\log(\overline{F_{10.7}}) \approx 4.4$ ).

We find that the variability driven by the geomagnetic indices captures most of the activity in that particular case; as expected the model does best at medium activity. However, our model underestimates the peak magnitude of the ionization rates during this period, by about a factor of 2 on the lower activity day (05 April 2010), and by about a factor of 3 to 4 on the day of largest activity. For comparison we also show electron ionization rates from the Atmospheric Ionization during Substorm Model (AISstorm).

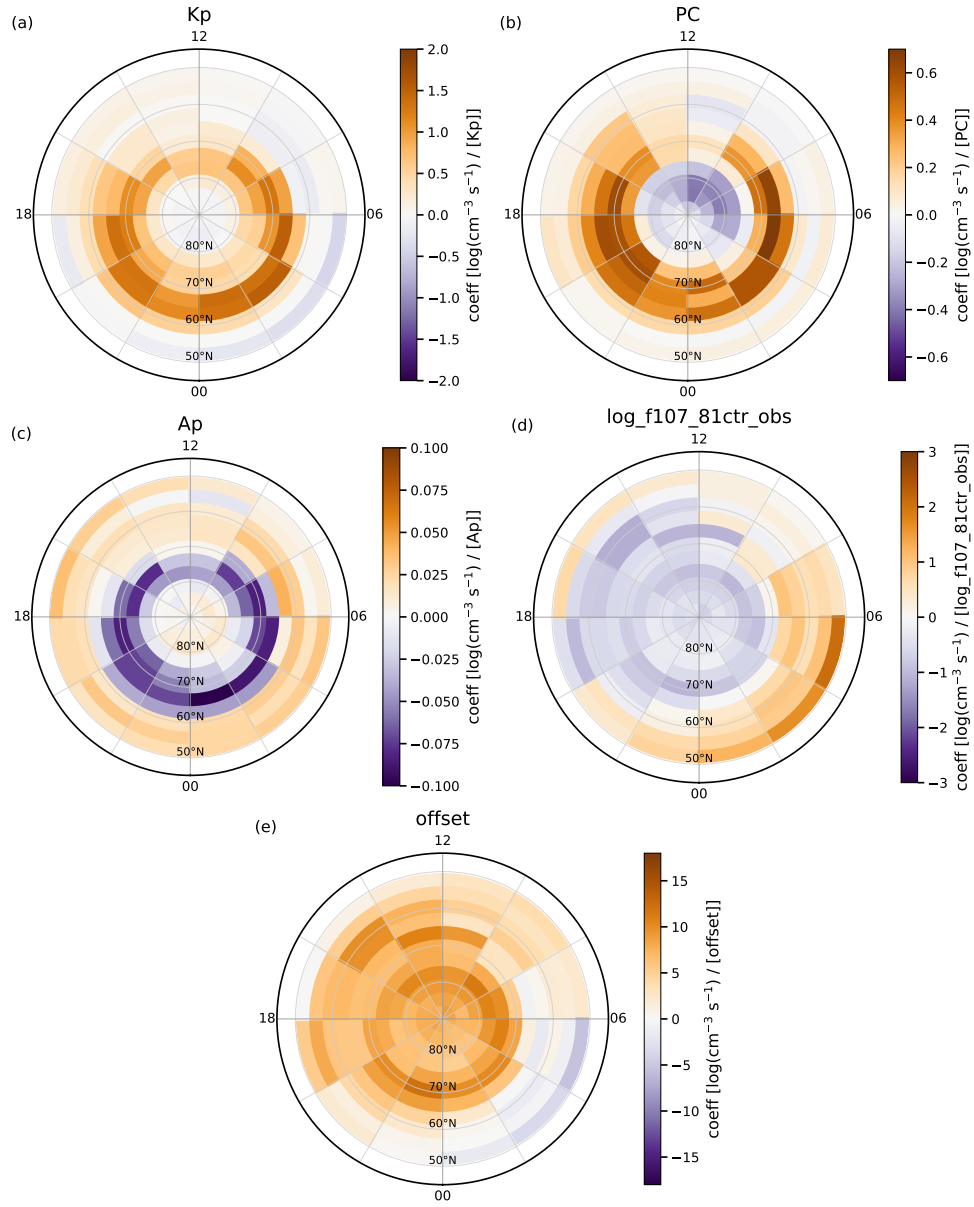


**Figure 3.** Fitted regression coefficients in the NH per MLT and geomagnetic latitude, (a) Kp, (b) PC, (c) Ap, (d)  $\log(\bar{F}_{10.7})$ , and (e) offset.

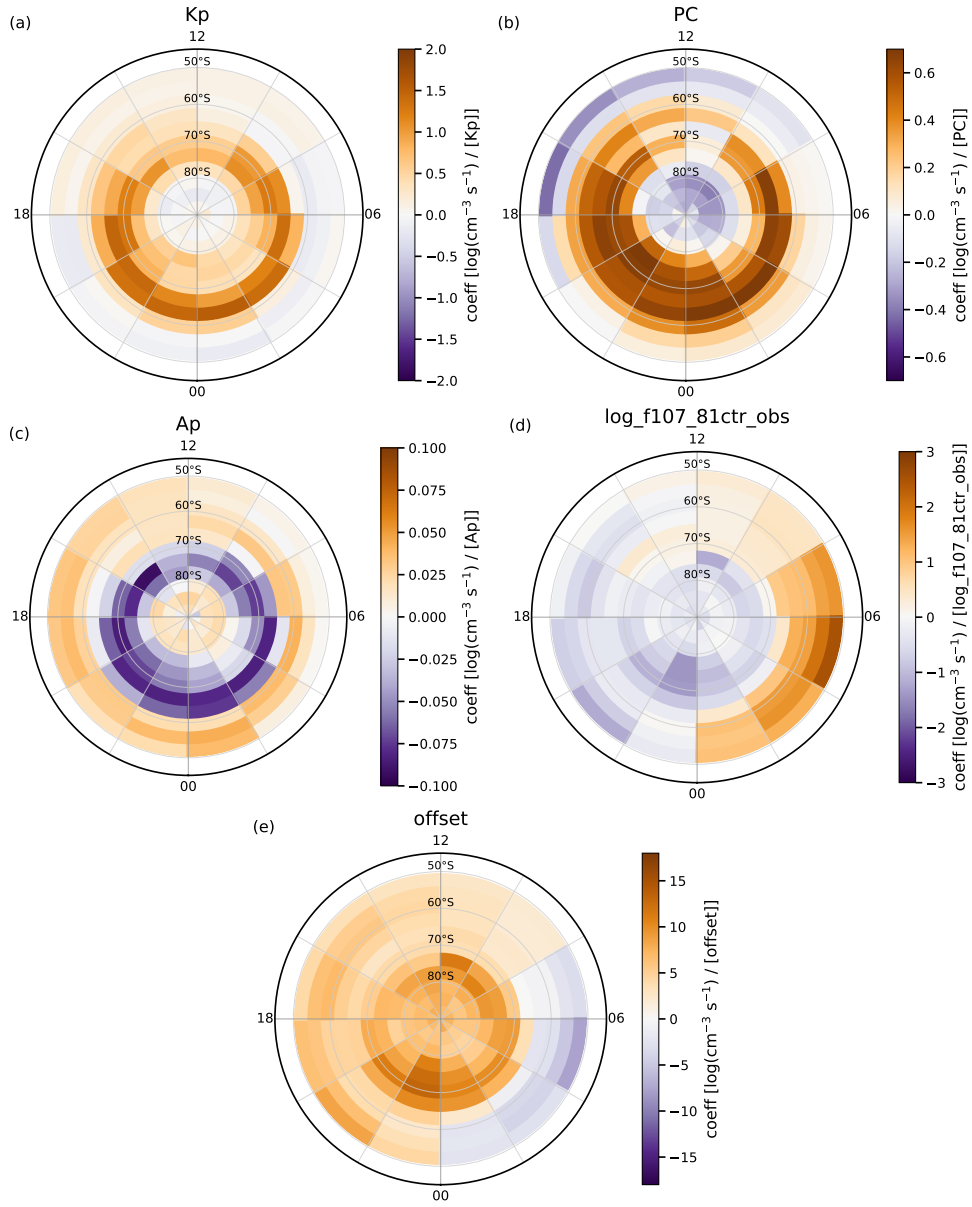


**Figure 4.** Fitted regression coefficients in the SH per MLT and geomagnetic latitude, (a) Kp, (b) PC, (c) Ap, (d)  $\log(\overline{F}_{10.7})$ , and (e) offset.



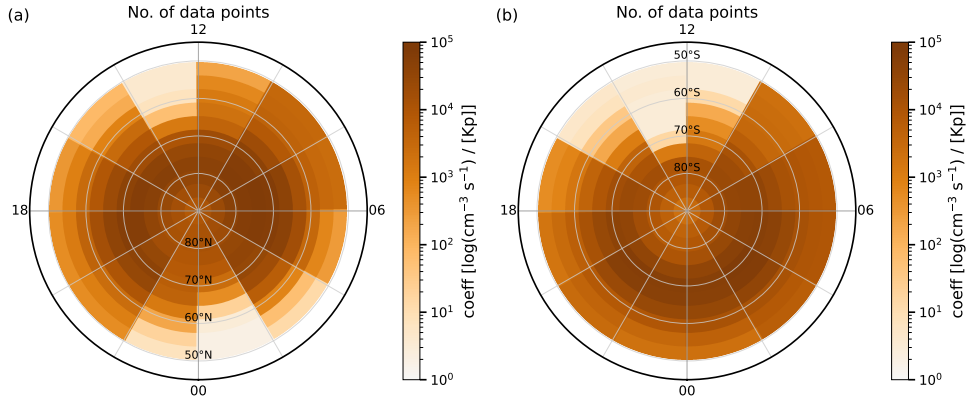


**Figure 5.** Distribution of available data points used for fitting, (a) Northern Hemisphere, (b) Southern Hemisphere.

AISstorm is based on AIMOS (Wissing & Kallenrode, 2009), augmented by several improvements, mainly a geomagnetic grid, substorm dependence, and a particle specific polar cap size (Yakovchuk & Wissing, 2023). AISstorm uses 18 years of POES and Metop satellite data (2001–2018), categorized by Kp level and substorm activity, and by geomagnetic APEX location (Richmond, 1995) and MLT with up to  $1^\circ$  latitude by  $3.75^\circ$  longitude resolution. Typical average flow maps are presented in Yakovchuk and Wissing (2019). Here the AISstorm ionization rates are averaged to 2 h MLT resolution to match our model. We find that the ionization rates from AISstorm differ from our model with peak rates of about a factor of 5 lower. They also peak at higher altitudes, about 110 km compared to around 105 km from our model. While the comparison in Fig. 6 shows single profiles at a particular location and time, a more statistical comparison shows that the peak ionization rates of both models are rather similar (not shown here).

#### 4.5 Discussion

The fit and residuals shown in Figs. 1 and 2 show some remaining variability on top of white noise. However, adding (semi-)annual harmonics or more proxies to the regressors did not improve the fit quality in a way that would have justified the increase in number of model parameters.

The choice to include both Kp and Ap comes about because both capture geomagnetic activity with different scales. Kp is quasi-logarithmic, and Ap quasi-linear. Adding yet another activity index, PC, has the advantage of capturing that activity with a higher time resolution, 1-h (PC) on top of the 3-h variability from Kp and Ap. The general 11-year solar cycle activity is included via the 81-day averaged 10.7 cm radio flux, effectively sampled daily.

The DMSP/SSUSI orbits are sun-synchronous which means they sample approximately the same latitude/MLT region every orbit, leading to worse sampling in certain areas, see Fig. 5. We try to mitigate this low sampling by limiting the number of proxies as well as the geomagnetic latitude range of the model. However, in some of the bins the number of usable data points is still small, and the fit resulted in ambiguous coefficients. In those cases, we use bilinear interpolation from the surrounding grid cells. Note that auroral activity and therefore the atmospheric ionization is typically constrained to a particular region, and interpolating or extrapolating to regions without enough data points might result in non-optimal predictions.

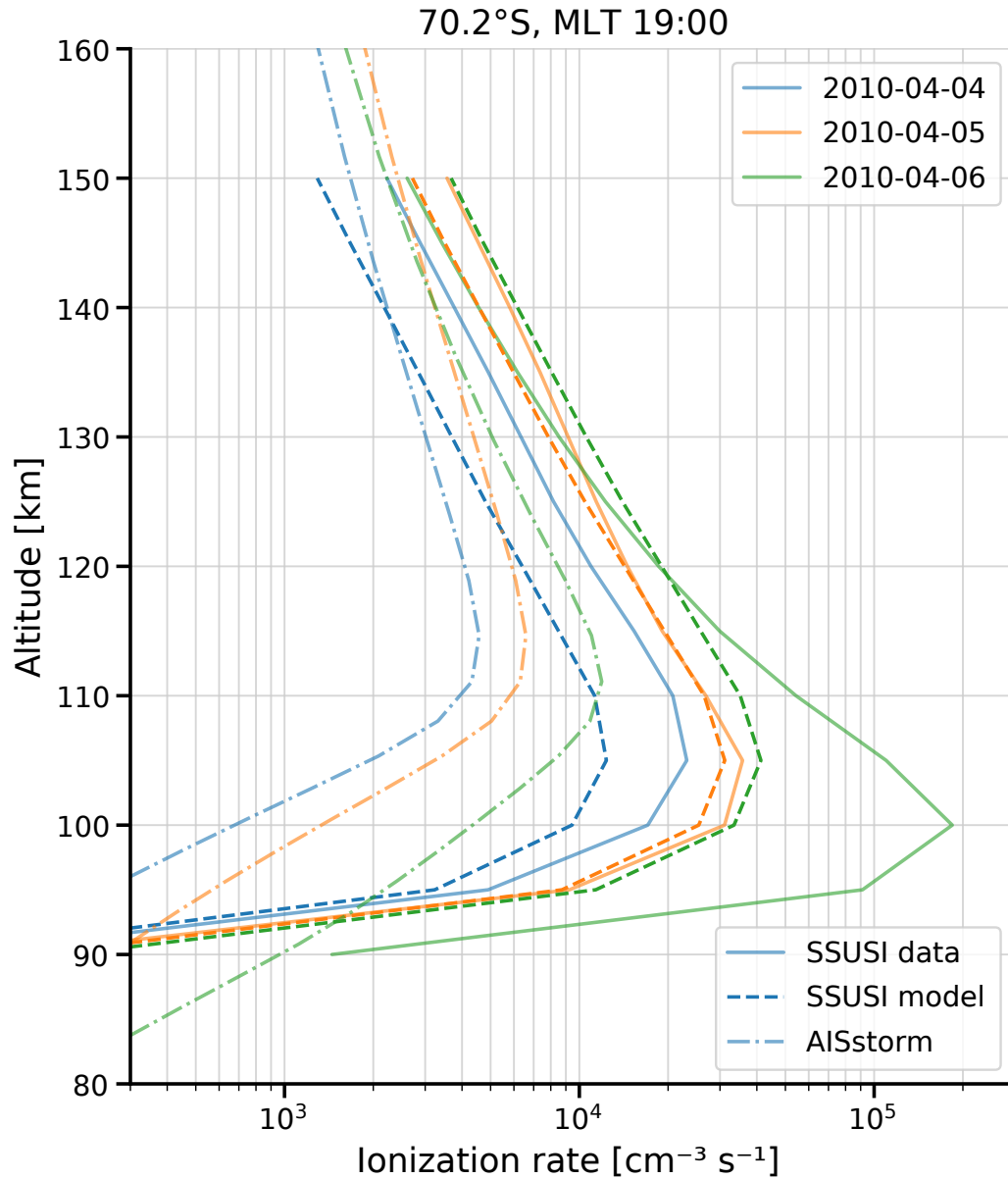


**Figure 6.** Daily-averaged ionization rate profiles during a substorm event in April 2010 (Tyssøy et al., 2021; Sinnhuber et al., 2021) for a selected geomagnetic latitude/MLT bin. Shown are the SSUSI-derived profiles (solid), the profiles from the model (current work; dashed), and the preliminary AISstorm profiles (dash-dotted).

The choice to cut off very low ionization rates is a purely subjective one, and the exact value might be subject to further fine tuning. Similarly, higher resolution in MLT and geomagnetic latitude is also possible, but both would require reprocessing of the data. Higher vertical resolution could be obtained by interpolating the 5-km  $\log(q)$  values supplied by the model, along with cubic-spline interpolation of  $\log(q)$  to a finer grid.

We use the energy range as given in the SSUSI data files, which is limited to 2–20 keV because of the method used (see, e.g. Knight et al., 2018). We use a single Maxwellian or Gaussian spectrum based on Bender et al. (2021), and no special attempt is made to include different spectral shapes, e.g. including a high-energy tail (see, e.g. Strickland et al., 1993). This may underestimate the true ionization rates at altitudes below about 95 km slightly, but as has been shown, compared to EISCAT they are still within the range of variability (Bender et al., 2021).

The validation against ground-based measurements is naturally limited in location. In our model we extend these results globally, there are no transition MLTs and we use the same spectra for all latitudes. Since the comparison study covers a wide range of magnetic local times, separating the pre- and post-midnight sectors seems justified. However, the extension to all latitudes is an assumption that might skew the predictions in cases it is violated.

## 5 Conclusions

We present an empirical model of auroral ionization rates derived from 12 (10) years of DMSP/SSUSI F17 (F18) observations. The ionization rate profiles are derived from the average electron energy and energy flux used as input to the ionization rate parametrization by (Fang et al., 2010), using NRLMSISE-00 (Picone et al., 2002) as the background neutral atmosphere and the energy spectra as determined by our validation study (Bender et al., 2021). The model is based on the time series of these profiles binned in 2-h MLT and 3.6° geomagnetic latitude and calculated at 5-km altitude steps from 90 to 150 km. For each altitude we derived a map of regression coefficients for Kp, PC, Ap,  $\log(\overline{F_{10.7}})$ , and a constant offset.

The choice of proxies has been empirically determined, taking also into account the availability and how well the indices are maintained. When setting up the model, AE and Dst were other possible choices. However, data for both indices were only available until February 2018 and not suitable to fit the whole time series, even less so for predicting ionization rates for chemistry–climate models. Of course this caution of index availability also applies to the ones used in this study, especially the more rarely used PC index. Currently, the OMNI database is well-maintained in that regard, which gives us confidence that the choice we made here is also future proof. On the other hand, Kp accounted for the majority of the variability, and it is one of the widest used and most accessible geomagnetic indices so that this would be the index of choice if the number of proxies needs to be limited further.

## Appendix A Model application

The application of the model to retrieve the ionization rates should be rather straightforward:

1. Acquire the 1-h sampled proxy values for the UT time in question, for example from the OMNI database (Papitashvili & King, 2020).
2. If not already available, calculate the geomagnetic latitude and magnetic local time for your location and time.
3. Retrieve the proxy coefficients from the coefficient table file for the grid cell containing the location calculated in the previous step, i.e. the closest grid cell cen-

- tre as given in the table. If preferred, bilinear interpolation in magnetic local time and geomagnetic latitude can be used to calculate the coefficients and their variances for the location in question. Optionally, retrieve the respective coefficients for all 5-km altitude steps for later interpolation.
4. Multiply the proxy coefficients by the proxy values.
  5. Sum over the proxies and add the offset to obtain (the logarithm of) the ionization rate at the required altitude. Steps 4 and 5 are the practical implementation of Eq. (1).
  6. (optional) Use cubic (3rd-order) spline interpolation of  $\log(q)$  in altitude to obtain a finer resolution of the ionization rate profile.
  7. (optional) Repeat steps 3 to 5, replace the proxy coefficients by the ones for the standard deviation of the coefficients, and square the results before summing the terms, to obtain an estimate for the (squared) uncertainty of  $\log(q)$ .

## Open Research Section

The SSUSI data used in this study are available at [https://ssusi.jhuapl.edu/data\\_products](https://ssusi.jhuapl.edu/data_products) (SSUSI, 2020). The source code to calculate the ionization rates and the empirical model is available as a Python software package distributed under the GPLv2 license (Bender, 2023).

## Acknowledgments

Stefan Bender and Patrick J. Espy acknowledge support from the Birkeland Center for Space Sciences (BCSS), supported by the Research Council of Norway under grant number 223252/F50. Stefan Bender also acknowledges financial support from the Agencia Estatal de Investigacion, MCIN/AEI/10.13039/501100011033, through grants PID2022-141216NB-I00 and CEX2021-001131-S. Larry J. Paxton is the principal investigator of the SSUSI project, funded by the Air Force Defense Meteorological Satellite Program contract N00024-22-D-6404. We acknowledge use of NASA/GSFC’s Space Physics Data Facility’s OMNIWeb service and OMNI data. The computations were performed on resources provided by UNINETT Sigma2 - the National Infrastructure for High Performance Computing and Data Storage in Norway. We thank J. M. Wissing for providing the AISstorm data, the development of AISstorm was funded by the German Science Foundation (DFG project WI4417/2-1).

## References

- Bender, S. (2023, September). *st-bender/pyeppaurora: Version 0.3.0*. Zenodo [code]. Zenodo. Retrieved from <https://zenodo.org/record/8334549> doi: 10.5281/zenodo.8334549
- Bender, S., Espy, P. J., & Paxton, L. J. (2021, October). Validation of SSUSI-derived auroral electron densities: comparisons to EISCAT data. *Ann. Geophys.*, *39*(5), 899–910. Retrieved from <https://angeo.copernicus.org/articles/39/899/2021/> doi: 10.5194/angeo-39-899-2021
- Fang, X., Randall, C. E., Lummerzheim, D., Wang, W., Lu, G., Solomon, S. C., & Frahm, R. A. (2010, November). Parameterization of monoenergetic electron impact ionization. *Geophys. Res. Lett.*, *37*(22), L22106. doi: 10.1029/2010gl045406
- Funke, B., Ball, W., Bender, S., Gardini, A., Harvey, V. L., Lambert, A., . . . Yushkov, V. (2017, March). HEPPA-II model-measurement intercomparison project: EPP indirect effects during the dynamically perturbed NH winter 2008–2009. *Atmos. Chem. Phys.*, *17*(5), 3573–3604. Retrieved from <http://www.atmos-chem-phys.net/17/3573/2017/> doi: 10.5194/acp-17-3573-2017

- Funke, B., López-Puertas, M., Gil-López, S., von Clarmann, T., Stiller, G. P., Fischer, H., & Kellmann, S. (2005, December). Downward transport of upper atmospheric NO<sub>x</sub> into the polar stratosphere and lower mesosphere during the Antarctic 2003 and Arctic 2002/2003 winters. *J. Geophys. Res. Atmos.*, *110*(D24), D24308. doi: 10.1029/2005JD006463
- Funke, B., López-Puertas, M., Stiller, G. P., & von Clarmann, T. (2014). Mesospheric and stratospheric NO<sub>y</sub> produced by energetic particle precipitation during 2002–2012. *J. Geophys. Res. Atmos.*, *119*(7), 4429–4446. doi: 10.1002/2013JD021404
- King, J. H., & Papitashvili, N. E. (2005, February). Solar wind spatial scales in and comparisons of hourly Wind and ACE plasma and magnetic field data. *J. Geophys. Res. Space Phys.*, *110*(A2), A02104. doi: 10.1029/2004ja010649
- Knight, H. K., Galkin, I. A., Reinisch, B. W., & Zhang, Y. (2018, July). Auroral Ionospheric E Region Parameters Obtained From Satellite-Based Far Ultraviolet and Ground-Based Ionosonde Observations: Data, Methods, and Comparisons. *J. Geophys. Res. Space Phys.*, *123*(7), 6065–6089. Retrieved from <https://agupubs.onlinelibrary.wiley.com/doi/full/10.1029/2017JA024822> doi: 10.1029/2017ja024822
- Mandea, M., & Korte, M. (Eds.). (2011). *Geomagnetic observations and models* (Vol. 5) (No. 1). doi: 10.1007/978-90-481-9858-0
- Matthes, K., Funke, B., Andersson, M. E., Barnard, L., Beer, J., Charbonneau, P., ... Versick, S. (2017, June). Solar forcing for CMIP6 (v3.2). *Geosci. Model Dev.*, *10*, 2247–2302. Retrieved from <http://www.geosci-model-dev.net/10/2247/2017/> doi: 10.5194/gmd-10-2247-2017
- Newell, P. T., Sotirelis, T., & Wing, S. (2009, September). Diffuse, monoenergetic, and broadband aurora: The global precipitation budget. *J. Geophys. Res. Space Phys.*, *114*(A9), A09207. doi: 10.1029/2009ja014326
- Newell, P. T., Wing, S., & Meng, C. (2005, November). Spectral properties and source regions of dayside electron acceleration events. *J. Geophys. Res. Space Phys.*, *110*(A11), A11205. doi: 10.1029/2005ja011264
- Papitashvili, N. E., & King, J. H. (2020). *OMNI Hourly Data*. [Data Set]. NASA Space Physics Data Facility. (Accessed on 23 February 2023) doi: 10.48322/1shr-ht18
- Paxton, L. J., Meng, C.-I., Fountain, G. H., Ogorzalek, B. S., Darlington, E. H., Gary, S. A., ... Smith, B. E. (1992, June). Special sensor ultraviolet spectrographic imager: an instrument description. In S. Chakrabarti & A. B. Christensen (Eds.), *Instrumentation for planetary and terrestrial atmospheric remote sensing*. SPIE. Retrieved from <https://www.spiedigitallibrary.org/conference-proceedings-of-spie/1745/0000/Special-sensor-ultraviolet-spectrographic-imager-an-instrument-description/> 10.1117/12.60595.full doi: 10.1117/12.60595
- Paxton, L. J., Schaefer, R. K., Zhang, Y., & Kil, H. (2017, February). Far ultraviolet instrument technology. *J. Geophys. Res. Space Phys.*, *122*(2), 2706–2733. Retrieved from <https://agupubs.onlinelibrary.wiley.com/doi/full/10.1002/2016JA023578> doi: 10.1002/2016ja023578
- Paxton, L. J., Schaefer, R. K., Zhang, Y., Kil, H., & Hicks, J. E. (2018, October). SSUSI and SSUSI-Lite: Providing Space Situational Awareness and Support for Over 25 Years [Article]. *Johns Hopkins APL Tech. Dig.*, *34*(3), 388–400.
- Picone, J. M., Hedin, A. E., Drob, D. P., & Aikin, A. C. (2002, December). Nrlmsise-00 empirical model of the atmosphere: Statistical comparisons and scientific issues. *J. Geophys. Res. Space Phys.*, *107*(A12), 1468. doi: 10.1029/2002JA009430
- Pérot, K., & Orsolini, Y. J. (2021, July). Impact of the major SSWs of february 2018 and january 2019 on the middle atmospheric nitric oxide abundance. *J. Atmos. Sol. Terr. Phys.*, *218*, 105586. doi: 10.1016/j.jastp.2021.105586

- Pérot, K., Urban, J., & Murtagh, D. P. (2014). Unusually strong nitric oxide descent in the Arctic middle atmosphere in early 2013 as observed by Odin/SMR. *Atmos. Chem. Phys.*, *14*(15), 8009–8015. Retrieved from <http://www.atmos-chem-phys.net/14/8009/2014/> doi: 10.5194/acp-14-8009-2014
- Randall, C. E., Harvey, V. L., Siskind, D. E., France, J., Bernath, P. F., Boone, C. D., & Walker, K. A. (2009). Nox descent in the arctic middle atmosphere in early 2009. *Geophys. Res. Lett.*, *36*(18), L18811. doi: 10.1029/2009GL039706
- Richmond, A. D. (1995). Ionospheric Electrodynamics Using Magnetic Apex Coordinates. *J. Geomagn. Geoelec.*, *47*(2), 191–212. Retrieved from <http://adsabs.harvard.edu/abs/1995JGG...47..191R> doi: 10.5636/jgg.47.191
- Sinnhuber, M., Tyssoy, H. N., Asikainen, T., Bender, S., Funke, B., Hendrickx, K., ... Yakovchuk, O. S. (2021, December). Heppa III Intercomparison Experiment on Electron Precipitation Impacts: 2. Model-Measurement Intercomparison of Nitric Oxide (NO) During a Geomagnetic Storm in April 2010. *J. Geophys. Res. Space Phys.*, *126*, e2021JA029466. doi: 10.1029/2021ja029466
- Smith-Johnsen, C., Marsh, D. R., Orsolini, Y., Tyssøy, H. N., Hendrickx, K., Sandanger, M. I., ... Stordal, F. (2018, June). Nitric Oxide Response to the April 2010 Electron Precipitation Event: Using WACCM and WACCM-D With and Without Medium-Energy Electrons. *J. Geophys. Res. Space Phys.*, *123*(6), 5232–5245. doi: 10.1029/2018ja025418
- SSUSI. (2020, September). *Data products*. available at: [https://ssusi.jhuapl.edu/data\\_products](https://ssusi.jhuapl.edu/data_products). (last access: 21 September)
- Strickland, D. J., Daniell, R. E., Jasperse, J. R., & Basu, B. (1993, December). Transport-Theoretic Model for the Electron-Proton-Hydrogen Atom Aurora, 2. Model Results. *J. Geophys. Res. Space Phys.*, *98*(A12), 21533–21548. doi: 10.1029/93ja01645
- Strickland, D. J., Jasperse, J. R., & Whalen, J. A. (1983). Dependence of auroral FUV emissions on the incident electron spectrum and neutral atmosphere. *J. Geophys. Res. Space Phys.*, *88*(A10), 8051. doi: 10.1029/ja088ia10p08051
- Troshichev, O., Andrezen, V., Vennerstrøm, S., & Friis-Christensen, E. (1988, November). Magnetic activity in the polar cap—a new index. *Planet. Space Sci.*, *36*(11), 1095–1102. Retrieved from <https://www.sciencedirect.com/science/article/pii/0032063388900633> doi: 10.1016/0032-0633(88)90063-3
- Troshichev, O., Dmitrieva, N., & Kuznetsov, B. (1979, March). Polar cap magnetic activity as a signature of substorm development. *Planet. Space Sci.*, *27*(3), 217–221. Retrieved from <https://www.sciencedirect.com/science/article/pii/0032063379900631> doi: 10.1016/0032-0633(79)90063-1
- Tyssoy, H. N., Sandanger, M. I., Ødegaard, L.-K. G., Stadsnes, J., Aasnes, A., & Zawedde, A. E. (2016, May). Energetic electron precipitation into the middle atmosphere—constructing the loss cone fluxes from MEPED POES. *J. Geophys. Res. Space Phys.*, *121*(6), 5693–5707. doi: 10.1002/2016ja022752
- Tyssoy, H. N., Sinnhuber, M., Asikainen, T., Bender, S., Clilverd, M. A., Funke, B., ... Yakovchuk, O. (2021, December). HEPPA III Intercomparison Experiment on Electron Precipitation Impacts: 1. Estimated Ionization Rates During a Geomagnetic Active Period in April 2010. *J. Geophys. Res. Space Phys.*, *126*, e2021JA029128. doi: 10.1029/2021ja029128
- van de Kamp, M., Rodger, C. J., Seppälä, A., Clilverd, M. A., & Verronen, P. T. (2018, September). An updated model providing long-term data sets of energetic electron precipitation, including zonal dependence. *J. Geophys. Res. Atmos.*, *123*(17), 9891–9915. doi: 10.1029/2017jd028253
- van de Kamp, M., Seppälä, A., Clilverd, M. A., Rodger, C. J., Verronen, P. T., & Whittaker, I. C. (2016, October). A model providing long-term data sets of energetic electron precipitation during geomagnetic storms. *J. Geophys. Res. Atmos.*, *121*(20), 12,520–12,540. doi: 10.1002/2015jd024212

- Wissing, J. M., & Kallenrode, M.-B. (2009, June). Atmospheric Ionization Module Osnabrück (AIMOS): A 3-D model to determine atmospheric ionization by energetic charged particles from different populations. *J. Geophys. Res. Space Phys.*, *114*(A6), A06104. doi: 10.1029/2008ja013884
- Wit, E., van den Heuvel, E., & Romeijn, J.-W. (2012, July). ‘All models are wrong...’: an introduction to model uncertainty. *Stat. Neerl.*, *66*(3), 217–236. doi: 10.1111/j.1467-9574.2012.00530.x
- Yakovchuk, O., & Wissing, J. M. (2019, November). Magnetic local time asymmetries in precipitating electron and proton populations with and without substorm activity. *Ann. Geophys.*, *37*(6), 1063–1077. doi: 10.5194/angeo-37-1063-2019
- Yakovchuk, O., & Wissing, J. M. (2023). Polar particle flux distribution and its spatial extent. *J. Space Weather Space Clim.*, *13*, 9. doi: 10.1051/swsc/2023009